

PIDM-DP: Physics-Informed Diffusion with Dormand-Prince Integration for Chaotic System Identification and State Reconstruction across Multiple Dynamical Regimes

Shailendra Dabral
 Indian Institute of Technology Indore
 ms2404121005@iiti.ac.in

Abstract

Reconstructing continuous state trajectories of chaotic dynamical systems from sparse, noisy observations remains a fundamental open problem in nonlinear science. We introduce the **Physics-Informed Diffusion Model with Dormand-Prince Integration (PIDM-DP)**, which embeds a fully differentiable 5th-order Dormand-Prince (DP-RK45) ODE integrator directly into the reverse sampling loop of a Denoising Diffusion Probabilistic Model (DDPM). At each denoising step, physics residuals are back-propagated via automatic differentiation, constraining every generated trajectory to satisfy the system’s governing equations to 5th-order accuracy. A *linear-scheduled guidance* mechanism that ramps the physics weight from zero at high noise levels to its full value near the clean-data limit prevents the gradient explosions that cause naive physics-informed approaches to fail on stiff systems with Jacobian eigenvalues of order $O(10^3)$.

Evaluated across five benchmark systems of increasing complexity 3D Lorenz, 3D Rössler, 5D Hyperchaotic, 20D Lorenz-96, and the stiff 3D Rabinovich-Fabrikant at 10% observation density with additive Gaussian noise ($\sigma=0.05$), PIDM-DP achieves reconstruction RMSE improvements of up to $15.4\times$ over an unconstrained diffusion baseline and decisively outperforms the Ensemble Kalman Filter on stiff systems where ensemble covariance collapses. On the Rabinovich-Fabrikant out-of-distribution benchmark, PIDM-DP attains RMSE 0.1097 ± 0.0269 versus 0.9443 ± 0.5288 (unconstrained diffusion, $8.6\times$ worse) and 0.3561 ± 0.3040 (EnKF, $3.2\times$ worse), with $p<0.001$ in paired Wilcoxon tests ($N=30$). Topological validation via the Rosenstein Lyapunov estimator confirms that PIDM-DP preserves the chaotic invariant measure. The joint state-parameter representation enables implicit system identification, recovering the Rayleigh number with 5.3% mean absolute percentage error from 10% observations. PIDM-DP achieves the lowest mean RMSE against CSDI, GRU-ODE, and ESN baselines across all 10 in-distribution and out-of-distribution benchmarks.

Contributions. PIDM-DP embeds a differentiable DP-RK45 integrator into reverse diffusion sampling; linear-scheduled physics guidance prevents gradient explosions on stiff chaotic systems; on the Rabinovich-Fabrikant OOD benchmark the method improves RMSE by $8.6\times$ over unconstrained diffusion and $3.2\times$ over EnKF; it achieves the best mean RMSE across all 10 ID/OOD benchmarks against CSDI, GRU-ODE, and ESN; and Lyapunov plus parameter-recovery analyses support manifold-level fidelity.

1 Introduction

1.1 Motivation and Problem Setting

The problem of reconstructing a continuous state trajectory from a sparse, noisy measurement sequence is among the most practically consequential inverse problems in nonlinear science. In atmospheric physics, satellite overpasses deliver state measurements at intervals of approximately 90 minutes, each corrupted by instrument noise; a complete atmospheric state must be inferred from this sliver of information to initialise operational 72-hour forecasts [19]. In plasma physics, sparse magnetic probe arrays must reconstruct the full current distribution for real-time tokamak control [22]. In neuroscience, a handful of electrode recordings must capture whole-brain activity from spatially localised measurements [10]. In each setting the same mathematical challenge recurs: given $m \ll L$ noisy observations $\{y_1, \dots, y_m\}$ sampled from an L -step trajectory of a chaotic ODE, reconstruct the full continuous state $\mathbf{x}(t)$ and identify the hidden system parameters \mathbf{p} .

What distinguishes this from a standard regression or interpolation problem is the *butterfly effect* [31]. A 1% error in the reconstructed state at one observation grows by a factor of $e^{\lambda_{\max} \Delta t_{\text{gap}}}$ before the next observation arrives. For the Lorenz system with $\lambda_{\max} \approx 0.906$ and 90 unobserved steps at $\Delta t = 0.05$, this amplification exceeds 59-fold. Any method that does not actively enforce the governing ODE will generate trajectories that are statistically plausible but physically impossible.

1.2 Limitations of Existing Approaches

Ensemble Kalman Filter (EnKF). The EnKF [17, 8, 9] propagates an ensemble of states forward under the exact governing equations and applies Kalman corrections at each observation. As the operational gold standard for atmospheric data assimilation, it performs optimally under near-Gaussian, mildly nonlinear conditions. However, at extreme observation sparsity (90% missing data), three systematic limitations emerge: (i) the Gaussian error assumption distorts the fractal geometry of strange attractors; (ii) ensemble collapse occurs when the effective sample size is too small relative to the state dimension [14]; and (iii) for stiff systems such as the Rabinovich-Fabrikant equations, ensemble members entering the stiff manifold during unobserved integration windows generate covariance explosions that standard inflation techniques cannot recover [1].

Modern sequence and generative models, LSTMs, Echo State Networks, Transformers, Neural ODEs, and diffusion-based imputers [13, 16, 34, 3, 33] are powerful statistical interpolators that learn correlations rather than physics. As we demonstrate empirically across five benchmarks, a diffusion model trained on chaotic trajectories without physical constraints undergoes *Lyapunov collapse*: the maximal Lyapunov exponent of generated trajectories drops toward zero, indicating that the model has learned smooth, nearly-periodic orbits rather than genuine strange attractors.

Physics-Informed Neural Networks (PINNs). PINNs [23, 18] incorporate ODE residuals into the training loss but require per-trajectory optimisation, cannot provide amortised inference, and typically employ low-order numerical residuals that accumulate significant error on chaotic trajectories. Crucially, they provide no mechanism for applying physics constraints selectively during different phases of generative sampling.

1.3 The Present Contribution

We introduce **PIDM-DP** (Physics-Informed Diffusion Model with Dormand-Prince integration), which resolves all three failure modes through three tightly integrated innovations:

1. **Differentiable DP-RK45 residual.** A PyTorch-native six-stage Runge-Kutta implementation with explicit rational Butcher coefficients provides a 5th-order accurate physics gradient at every reverse diffusion step. The implementation achieves $< 10^{-14}$ absolute error against a NumPy reference integrator, validated before all experiments.
2. **Linear-scheduled guidance.** A time-varying physics weight $\lambda_{\text{phy}}(t) = \lambda_{\text{base}}(1 - t/T)$ suppresses physics corrections during the high-noise phase where off-manifold states produce meaningless and numerically destructive gradients, and applies the full constraint progressively as the sample converges toward the clean-data limit. This scheduling mechanism is, to our knowledge, the first solution to the stiffness-gradient instability that causes existing physics-informed diffusion approaches to fail on systems with Jacobian spectral radii of $O(10^2)$ – $O(10^3)$.
3. **Safe autograd manifold projection.** Gradient norm clipping combined with a graceful exception-handling fallback ensures the reverse diffusion degrades to standard DDPM rather than diverging when the integrator encounters a numerically singular state.

The framework further incorporates a *joint state-parameter representation* that co-generates trajectory reconstructions and hidden system parameter estimates in a single forward pass, without any direct parameter observations or per-trajectory retraining.

We evaluate PIDM-DP across five chaotic benchmarks at 10% observation density: the 3D Lorenz, 3D Rössler, 5D Hyperchaotic, 20D Lorenz-96, and the notoriously stiff 3D Rabinovich-Fabrikant systems. PIDM-DP achieves the lowest mean RMSE in all 10 in-distribution (ID) and out-of-distribution (OOD) benchmark conditions against CSDI, GRU-ODE, and ESN baselines, with 29 of 30 paired Wilcoxon tests significant at $p < 0.05$. On the stiff Rabinovich-Fabrikant system, PIDM-DP outperforms both the unconstrained diffusion baseline and the EnKF oracle by factors of $8.6\times$ and $3.2\times$, respectively.

1.4 Paper Organisation

Section 2 reviews chaotic dynamics, DDPMs, the Dormand-Prince method, and the EnKF, together with a discussion of related work. Section 3 introduces the five benchmark systems. Section 4 presents the PIDM-DP architecture and algorithms. Section 5 provides implementation details. Section 6 describes the experimental protocol. Section 7 presents and interprets the results. Section 8 concludes with limitations and future directions.

2 Background and Related Work

2.1 Chaotic Dynamical Systems and Lyapunov Exponents

A continuous autonomous dynamical system is governed by the initial-value problem:

$$\dot{\mathbf{x}} = f(\mathbf{x}, \mathbf{p}), \quad \mathbf{x}(t_0) = \mathbf{x}_0, \quad (1)$$

where $\mathbf{x}(t) \in \mathbb{R}^D$ is the state vector, $\mathbf{p} \in \mathbb{R}^P$ are fixed physical parameters, and $f : \mathbb{R}^D \times \mathbb{R}^P \rightarrow \mathbb{R}^D$ is the (smooth) vector field. A system is called *chaotic* when two initially infinitesimally close trajectories diverge exponentially in time:

$$\|\mathbf{x}(t) - \tilde{\mathbf{x}}(t)\| \approx \|\delta\mathbf{x}_0\| e^{\lambda_{\max} t}, \quad \lambda_{\max} > 0, \quad (2)$$

where λ_{\max} is the *maximal Lyapunov exponent (MLE)* [36]. For the Lorenz system at canonical parameters, $\lambda_{\max} \approx 0.906$ [7], and a 1% error at $t = 0$ grows to the full attractor scale in approximately five time units. All trajectories of a dissipative chaotic system ultimately reside on a *strange attractor*: a fractal invariant set with non-integer Hausdorff dimension (≈ 2.06 for Lorenz [11]).

A system is *hyperchaotic* if at least two Lyapunov exponents are positive [27]; it is *stiff* if its Jacobian $\partial f/\partial \mathbf{x}$ possesses eigenvalues of widely differing magnitudes, requiring prohibitively small explicit time-steps for numerical stability. The Rabinovich-Fabrikant equations exhibit Jacobian spectral radii of $O(10^2)$ – $O(10^3)$ near certain state-space regions, which is precisely what makes them a severe test for any physics-constrained generative method.

2.2 Denoising Diffusion Probabilistic Models (DDPMs)

Let $\mathbf{x}_0 \in \mathbb{R}^{D \times L}$ denote a clean chaotic trajectory. The DDPM *forward process* constructs a Markov chain that corrupts \mathbf{x}_0 with increasing Gaussian noise [29, 12]:

$$q(\mathbf{x}_t | \mathbf{x}_{t-1}) = \mathcal{N}\left(\mathbf{x}_t; \sqrt{1 - \beta_t} \mathbf{x}_{t-1}, \beta_t \mathbf{I}\right), \quad (3)$$

where $\{\beta_t\}_{t=1}^T$ is a fixed noise schedule. Defining $\bar{\alpha}_t = \prod_{i=1}^t (1 - \beta_i)$, the marginal collapses to the closed-form reparameterisation:

$$\mathbf{x}_t = \sqrt{\bar{\alpha}_t} \mathbf{x}_0 + \sqrt{1 - \bar{\alpha}_t} \boldsymbol{\epsilon}, \quad \boldsymbol{\epsilon} \sim \mathcal{N}(\mathbf{0}, \mathbf{I}). \quad (4)$$

A neural network $\boldsymbol{\epsilon}_\theta$ is trained to predict the injected noise:

$$\mathcal{L}_{\text{DDPM}} = \mathbb{E}_{\mathbf{x}_0, t, \boldsymbol{\epsilon}} \left[\left\| \boldsymbol{\epsilon} - \boldsymbol{\epsilon}_\theta(\sqrt{\bar{\alpha}_t} \mathbf{x}_0 + \sqrt{1 - \bar{\alpha}_t} \boldsymbol{\epsilon}, t) \right\|^2 \right]. \quad (5)$$

New samples are generated by iterating the learned reverse step:

$$\mathbf{x}_{t-1} = \frac{1}{\sqrt{\alpha_t}} \left(\mathbf{x}_t - \frac{1 - \alpha_t}{\sqrt{1 - \bar{\alpha}_t}} \boldsymbol{\epsilon}_\theta(\mathbf{x}_t, t) \right) + \sqrt{\beta_t} \mathbf{z}, \quad \mathbf{z} \sim \mathcal{N}(\mathbf{0}, \mathbf{I}). \quad (6)$$

Classifier/guidance-based approaches [5] augment Eq. (6) with an additional gradient correction:

$$\mathbf{x}_{t-1} \leftarrow \mathbf{x}_{t-1} - \eta \nabla_{\mathbf{x}_t} \mathcal{L}_{\text{guide}}, \quad (7)$$

where $\mathcal{L}_{\text{guide}}$ encodes data fidelity and any domain-specific physical constraints. PIDM-DP instantiates $\mathcal{L}_{\text{guide}}$ as a combination of sparse-observation fidelity and a fully differentiable ODE residual computed via DP-RK45.

2.3 The Dormand-Prince RK45 Method

For a generic first-order ODE $\dot{\mathbf{s}} = f(\mathbf{s}, \mathbf{p})$, the **Dormand-Prince RK45 method** [6] evaluates f at six intermediate stages k_1, \dots, k_6 and constructs a 5th-order accurate update:

$$\mathbf{s}_{n+1} = \mathbf{s}_n + \Delta t \left(\frac{35}{384} k_1 + \frac{500}{1113} k_3 + \frac{125}{192} k_4 - \frac{2187}{6784} k_5 + \frac{11}{84} k_6 \right), \quad (8)$$

with local truncation error $O(\Delta t^6)$ (see Appendix A for the full Butcher tableau). At $\Delta t = 0.05$, this yields a physics residual of magnitude $O((\Delta t)^5) \approx 3 \times 10^{-7}$, an order-of-magnitude improvement over classical RK4. The gradient of Eq. (8) with respect to the initial state \mathbf{s}_n is:

$$\frac{\partial \mathbf{s}_{n+1}}{\partial \mathbf{s}_n} = \mathbf{I} + \Delta t \sum_{i \in \{1, 3, 4, 5, 6\}} b_i \frac{\partial k_i}{\partial \mathbf{s}_n}, \quad (9)$$

where b_i are the 5th-order weights and each $\partial k_i/\partial \mathbf{s}_n$ is itself a composition of Jacobian evaluations along the stage computation graph. Our PyTorch-native implementation materialises this gradient exactly via automatic differentiation, with $< 10^{-14}$ absolute error against a NumPy reference.

An ODE is *stiff* if the largest Jacobian eigenvalue satisfies $|\lambda_J| \Delta t \gg 1$. For the Rabinovich-Fabrikant system, eigenvalues of $O(10^3)$ near certain state-space regions demand $\Delta t \lesssim 0.002$ for explicit stability, directly conflicting with the $\Delta t = 0.05$ used in the diffusion sampling loop. The linear-scheduled guidance introduced in Section 4.5 resolves this tension entirely.

2.4 Ensemble Kalman Filter

The EnKF [9] maintains N_e ensemble members $\{\mathbf{x}_i^f(t_k)\}_{i=1}^{N_e}$, propagates each forward under the exact ODE, and applies a Kalman analysis step at each observation time t_k :

$$\mathbf{x}_i^a = \mathbf{x}_i^f + \mathbf{K}_k \left(\mathbf{y}_k + \boldsymbol{\eta}_i - H(\mathbf{x}_i^f) \right), \quad \mathbf{K}_k = \mathbf{P}_k^f \mathbf{H}^\top \left(\mathbf{H} \mathbf{P}_k^f \mathbf{H}^\top + \mathbf{R} \right)^{-1}, \quad (10)$$

where H is the observation operator and \mathbf{R} is the measurement noise covariance. With 90% observation gaps and 50 ensemble members in a 20-dimensional state space, the sample covariance \mathbf{P}_k^f approaches singularity and filter divergence becomes increasingly likely [14]. Furthermore, the Gaussian Kalman correction distorts the non-Gaussian geometry of chaotic strange attractors [1].

2.5 Related Work

Physics-informed deep learning for dynamical systems has evolved along three largely separate lines. *Training-time physics constraints* (PINNs, 23; physics-constrained neural ODEs, 3) embed ODE residuals into the loss function and are optimised per trajectory, making them unsuitable for amortised inference at test time. *Observation-conditioned generative models* (CSDI, 33; score-based imputation methods) learn to impute missing time-series values but impose no physical constraints, leading to off-manifold drift under large observation gaps. *Reservoir-computing approaches* (Echo State Networks, 16, 21) can track chaotic attractors when observations are sufficiently dense but accumulate open-loop errors under the 90% sparsity studied here.

Diffusion models for physical systems have recently appeared in fluid dynamics [15], but these works assume dense spatial observations of PDE fields rather than sparse temporal measurements of ODE trajectories, and do not address stiff dynamics or implicit parameter identification. The combination of differentiable high-order ODE integration within the reverse diffusion loop, scheduled to avoid stiffness-induced gradient explosions, constitutes the primary technical novelty of the present work.

3 Benchmark Systems

We evaluate PIDM-DP on five systems chosen to probe increasing dimensionality, sensitivity, and stiffness. Figure 1 shows the ground-truth invariant manifolds for each.

3.1 Lorenz Attractor (3D)

$$\dot{x} = \sigma(y - x), \quad \dot{y} = x(\rho - z) - y, \quad \dot{z} = xy - \beta z. \quad (11)$$

At canonical parameters $(\sigma, \rho, \beta) = (10, 28, 8/3)$ this system exhibits a double-scroll strange attractor with $\lambda_{\max} \approx 0.906$ [19]. **Training:** $\sigma \in [8, 12]$, $\rho \in [20, 35]$, $\beta \in [2, 4]$. **OOD:** $\sigma \in [5, 8]$, $\rho \in [15, 20]$, $\beta \in [1.5, 2]$ (pre-chaotic boundary).

3.2 Rössler Attractor (3D)

$$\dot{x} = -y - z, \quad \dot{y} = x + ay, \quad \dot{z} = b + z(x - c). \quad (12)$$

At $(a, b, c) = (0.2, 0.2, 5.7)$, $\lambda_{\max} \approx 0.071$ [26]. **Training:** $a, b \in [0.15, 0.25]$, $c \in [5.0, 7.0]$. **OOD:** $a, b \in [0.10, 0.15]$, $c \in [3.5, 5.0]$.

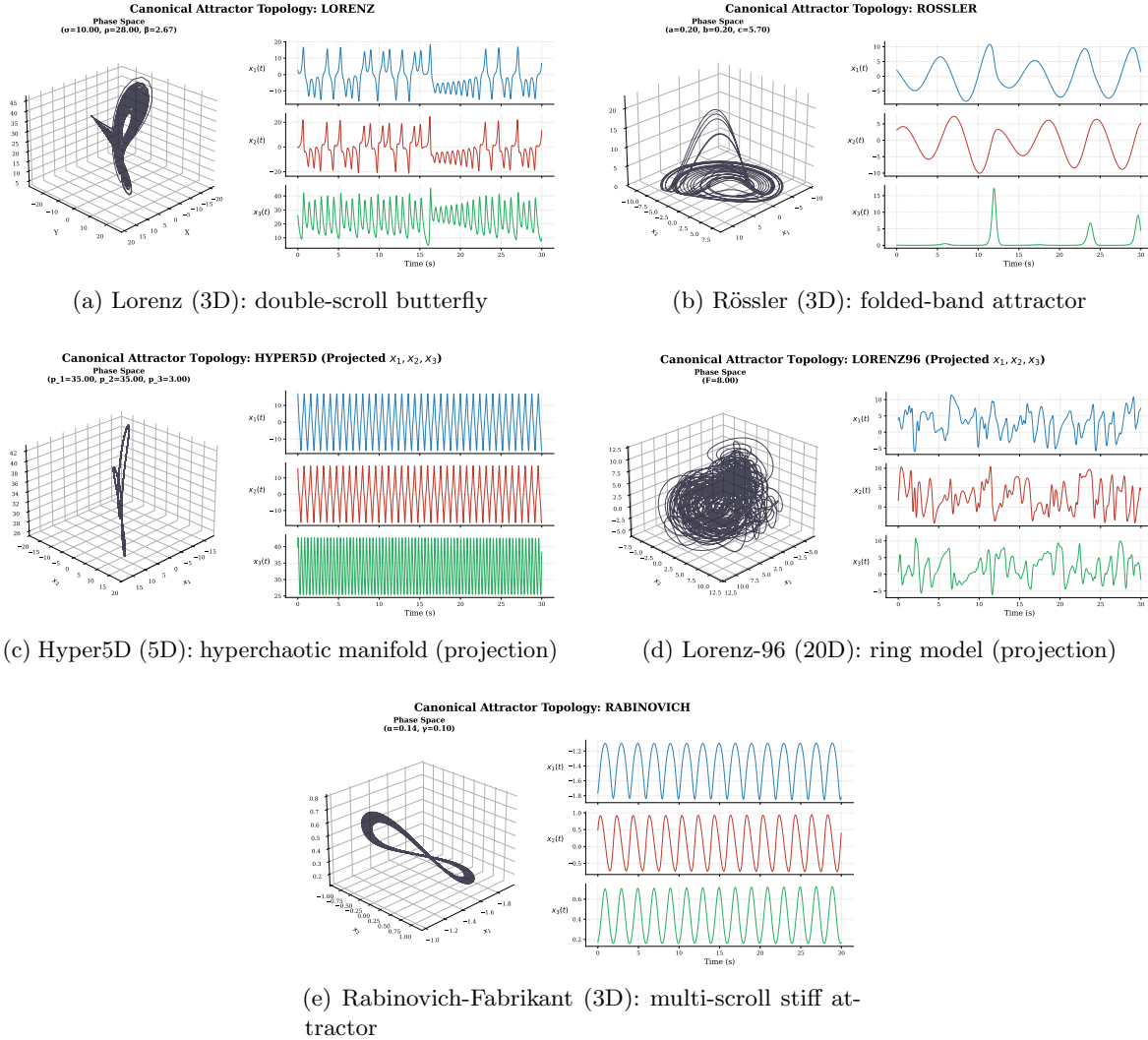


Figure 1: Ground-truth strange attractors for the five benchmark systems integrated with DOP853/LSODA at tight tolerances. The qualitatively distinct attractor geometries from the simple double-scroll of Lorenz to the topologically complex Rabinovich-Fabrikant multi-scroll present a systematic test of PIDM-DP’s ability to maintain physical fidelity across diverse regimes.

3.3 5D Hyperchaotic System

$$\begin{aligned}
\dot{x}_1 &= p_1(x_2 - x_1) + x_4, \\
\dot{x}_2 &= p_2x_1 - x_2 - x_1x_3 + x_5, \\
\dot{x}_3 &= x_1x_2 - p_3x_3, \\
\dot{x}_4 &= -x_1x_3 + 0.1x_4, \\
\dot{x}_5 &= -x_2x_3 + 0.1x_5.
\end{aligned} \tag{13}$$

This system is hyperchaotic (two positive Lyapunov exponents) [27]. **Training:** $p_1 \in [8, 12]$, $p_2 \in [20, 35]$, $p_3 \in [2, 4]$.

3.4 Lorenz-96 (20D)

$$\dot{x}_j = (x_{j+1} - x_{j-2})x_{j-1} - x_j + F, \quad j = 1, \dots, N, \quad N = 20, \tag{14}$$

with periodic boundary conditions. At $F = 8$ this system possesses approximately 13 positive Lyapunov exponents [20]. **Training:** $F \in [7, 9]$. **OOD:** $F \in [9, 11]$.

3.5 Rabinovich-Fabrikant Equations (3D, Stiff)

$$\dot{x} = y(z - 1 + x^2) + \gamma x, \quad \dot{y} = x(3z + 1 - x^2) + \gamma y, \quad \dot{z} = -2z(\alpha + xy). \tag{15}$$

Derived from plasma wave interactions [22], this system generates Jacobian eigenvalues of $O(10^3)$ near certain state-space regions, making it the most challenging benchmark for any explicit physics constraint. **Training:** $\alpha \in [0.10, 0.18]$, $\gamma \in [0.07, 0.13]$. **OOD:** $\alpha \in [0.20, 0.30]$, $\gamma \in [0.05, 0.09]$ (distinct bifurcation regime).

4 PIDM-DP Methodology

4.1 Problem Formulation

At each test trajectory, a random subset $\mathcal{O} \subset \{1, \dots, L\}$ with $|\mathcal{O}|/L = 0.10$ is observed with additive Gaussian noise:

$$\mathbf{y}_k = \mathbf{x}(t_k) + \boldsymbol{\eta}_k, \quad k \in \mathcal{O}, \quad \boldsymbol{\eta}_k \sim \mathcal{N}(\mathbf{0}, 0.05^2 \mathbf{I}). \tag{16}$$

The goal is to jointly (1) reconstruct the full trajectory $\hat{\mathbf{x}}(t)$ for all $t \in \{1, \dots, L\}$, (2) identify the hidden parameter vector $\hat{\mathbf{p}}$, and (3) ensure that the reconstructed attractor preserves the correct Lyapunov exponent $\lambda_{\max}(\hat{\mathbf{x}}) \approx \lambda_{\max}(\mathbf{x})$. No per-trajectory re-optimisation is permitted; inference must be amortised over the trained model.

4.2 Joint State-Parameter Representation

The central architectural innovation is treating system parameters as *constant spatial channels* broadcast across all time steps. For state dimension D_s and parameter dimension D_p , define the joint vector:

$$\mathbf{z}(t_k) = \begin{pmatrix} \mathbf{x}(t_k) \\ \mathbf{p} \end{pmatrix} \in \mathbb{R}^{D_s + D_p}, \tag{17}$$

giving a joint tensor $\mathbf{Z} \in \mathbb{R}^{(D_s + D_p) \times L}$ that serves as both the diffusion target and the network input during training. At inference, the denoised parameter channels converge to an estimate consistent

with the observed trajectory fragments. To prevent the network from absorbing step-by-step noise fluctuations into the parameter channels, we apply *parameter gradient pooling*:

$$\hat{\mathbf{p}}_{\text{pooled}} = \frac{1}{L} \sum_{k=1}^L \hat{\mathbf{p}}_k, \quad (18)$$

where $\hat{\mathbf{p}}_k$ is the denoised parameter estimate at time step k . This pooled vector is used for all physics guidance computations and is reported as the final parameter estimate at the conclusion of inference.

4.3 Temporal U-Net Architecture

The denoising backbone $\epsilon_\theta(\mathbf{Z}_t, t)$ is a 1D Temporal U-Net [24] adapted for chaotic multivariate time series:

- **Sinusoidal time embedding:** $\phi(t) \in \mathbb{R}^{128}$, followed by a two-layer MLP with SiLU activations, injected at every ResBlock as a learned bias.
- **Encoder:** Three stages with channel widths $64 \rightarrow 128 \rightarrow 256$, each comprising two ResBlock1D layers (two 1D convolutions, kernel size 3, GroupNorm, SiLU) and $2 \times$ average pooling between stages.
- **Bottleneck:** Two ResBlocks flanking a SelfAttention1D layer; this captures long-range temporal correlations necessary for matching local trajectory segments to global parameter estimates.
- **Decoder:** Symmetric to the encoder, with additive skip connections from the corresponding encoder stages; a final 1×1 convolution maps to $C = D_s + D_p$ output channels.

The total parameter count is approximately 2.9×10^6 across all five system configurations sufficient model capacity for trajectory lengths up to $L = 1000$ without overfitting, as confirmed by training/validation loss curves.

4.4 Differentiable DP-RK45 Physics Guidance

At each reverse diffusion step t , we first recover the predicted clean trajectory from the current noisy latent:

$$\hat{\mathbf{x}}_0 = \text{clamp} \left(\frac{\mathbf{x}_t - \sqrt{1 - \bar{\alpha}_t} \epsilon_\theta(\mathbf{x}_t, t)}{\sqrt{\bar{\alpha}_t}}, -3, 3 \right), \quad (19)$$

where the clamping to $[-3, 3]$ in normalised space prevents gradient blow-up at the first denoising steps. After denormalising to physical units via the stored training-set statistics $\mathcal{P}^{-1}(\cdot)$, we apply a DP-RK45 integration step to every pair of consecutive time indices in parallel:

$$\hat{\mathbf{s}}^{(k+1)} = \text{DP-RK45} \left(f, \mathbf{s}^{(k)}, \hat{\mathbf{p}}_{\text{pooled}}, \Delta t \right), \quad k = 0, \dots, L - 1. \quad (20)$$

The physics residual uses a logarithmically stabilised MSE to prevent gradient explosions when the predicted trajectory is far from the attractor manifold:

$$\mathcal{L}_{\text{phy}} = \log \left(1 + \text{MSE} \left(\hat{\mathbf{s}}^{(1:L)}, \hat{\mathbf{s}}_{\text{advanced}}^{(0:L-1)} \right) \right). \quad (21)$$

Simultaneously, a masked data-fidelity term constrains the reconstruction to the sparse observations in normalised space:

$$\mathcal{L}_{\text{data}} = \frac{1}{|\mathcal{O}|} \sum_{k \in \mathcal{O}} \left\| \hat{\mathbf{x}}_0^{(k)} - \mathbf{y}_k \right\|^2. \quad (22)$$

The total guidance loss is:

$$\mathcal{L}_{\text{total}} = w_{\text{data}} \mathcal{L}_{\text{data}} + \lambda_{\text{phy}}(t) \mathcal{L}_{\text{phy}}, \quad (23)$$

with $w_{\text{data}} = 150.0$. The guidance gradient $\mathbf{g} = -\nabla_{\mathbf{x}_t} \mathcal{L}_{\text{total}}$ flows via PyTorch autograd through the entire computational graph: $\mathbf{x}_t \rightarrow \hat{\mathbf{x}}_0 \rightarrow \mathcal{P}^{-1} \rightarrow \text{parameter pooling} \rightarrow \text{six-stage DP-RK45 evaluation} \rightarrow \mathcal{L}_{\text{phy}}$. Since every operation in this chain is a composition of differentiable tensor operations, no finite-difference approximation is required.

4.5 Linear-Scheduled Guidance: Resolving the Stiffness Crisis

The stiffness problem. At diffusion step $t \approx T$, the state \mathbf{x}_t is nearly pure Gaussian noise with values far from the attractor manifold. For the Rabinovich-Fabrikant system, evaluating $f(\mathbf{x}_t, \hat{\mathbf{p}})$ at such off-manifold points produces vector-field derivatives of $O(10^5)$, generating physics loss gradients that are simultaneously enormous in magnitude and physically meaningless in direction, a condition that causes immediate divergence of the reverse diffusion.

We resolve this fundamental tension by introducing a time-dependent physics weight:

$$\lambda_{\text{phy}}(t) = \lambda_{\text{base}} \cdot \left(1 - \frac{t}{T}\right), \quad (24)$$

which equals zero at $t = T$ (physics fully disabled at peak noise) and λ_{base} at $t = 0$ (full physics constraint at the clean-data limit). This linear ramp has a natural operational interpretation: during the first $\sim 80\%$ of the reverse process, the neural network freely establishes the gross attractor topology guided solely by the data-fidelity term $w_{\text{data}} \mathcal{L}_{\text{data}}$. As the diffusion step approaches zero and the predicted trajectory becomes interpretable as a physical orbit, the DP-RK45 residual progressively locks the trajectory onto the correct attractor manifold. Figure 2 illustrates the schedule.

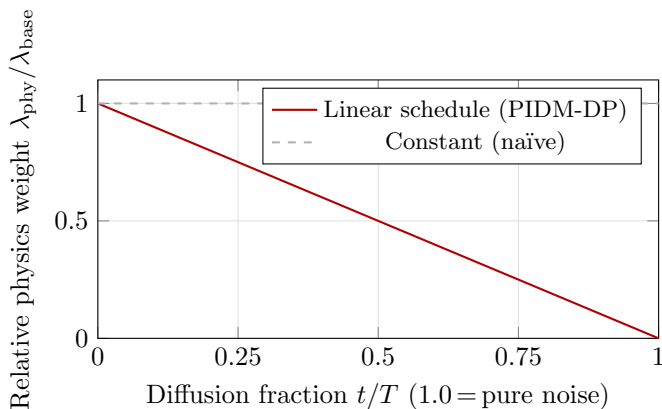


Figure 2: The linear physics guidance schedule of Eq. (24). The constraint is identically zero at peak noise (right) and fully active as the sample converges toward the clean-data limit (left). The naïve constant-weight baseline applies the full physics constraint to off-manifold Gaussian noise states, producing pathologically large and directionless gradients for stiff systems.

Per-system values of λ_{base} are selected based on a five-point ablation sweep (Section 7.5): Lorenz and Rössler = 2.0 (smooth, well-conditioned); Hyper5D = 1.5 (two positive Lyapunov exponents, moderate coupling); Lorenz-96 = 0.1 (high-dimensional; the diffusion model captures the manifold well through data fidelity alone); and Rabinovich-Fabrikant = 0.5 (stiff; conservative weight required).

4.6 Safe Autograd Manifold Projection

After computing the raw guidance gradient $\mathbf{g} = \nabla_{\mathbf{x}_t} \mathcal{L}_{\text{total}}$, we apply:

$$\mathbf{g}_{\text{safe}} = \begin{cases} \mathbf{0} & \text{if } \mathcal{L}_{\text{phy}} > 10^4, \\ -\frac{\mathbf{g}}{\|\mathbf{g}\| + \epsilon} \cdot \min(\|\mathbf{g}\|, g_{\text{thresh}}) & \text{otherwise,} \end{cases} \quad (25)$$

with clipping threshold $g_{\text{thresh}} = 0.15$ and $\epsilon = 10^{-8}$. The entire guidance computation is enclosed in a `try-except` block; any numerical exception (NaN, Inf, integrator failure) degrades the current step gracefully to a standard DDPM reverse step without guidance. This fallback ensures that the reverse diffusion is monotonically as good as the unconstrained baseline even in pathological cases.

Algorithm 1 presents the complete sampling procedure.

Algorithm 1 PIDM-DP: Physics-Informed Reverse Diffusion Sampling

Require: Trained ϵ_θ , noise schedule $\{\beta_t\}_{t=1}^T$, normalisation statistics \mathcal{P} , vector field f , observations \mathbf{y} , mask \mathbf{m} , physics base weight λ_{base}

- 1: Sample $\mathbf{x}_T \sim \mathcal{N}(\mathbf{0}, \mathbf{I})$
 - 2: **for** $t = T, T-1, \dots, 1$ **do**
 - 3: $\hat{\epsilon} \leftarrow \epsilon_\theta(\mathbf{x}_t, t)$
 - 4: $\hat{\mathbf{x}}_0 \leftarrow \text{clamp}\left(\frac{\mathbf{x}_t - \sqrt{1 - \alpha_t} \hat{\epsilon}}{\sqrt{\alpha_t}}, -3, 3\right)$
 - 5: Compute DDPM reverse mean $\boldsymbol{\mu}_t$ from $(\mathbf{x}_t, \hat{\epsilon})$
 - 6: Sample $\mathbf{x}_{t-1} \sim \mathcal{N}(\boldsymbol{\mu}_t, \beta_t \mathbf{I})$
 - 7: $\lambda_{\text{phy}} \leftarrow \lambda_{\text{base}}(1 - t/T)$
 - 8: **if** $\lambda_{\text{phy}} > 0$ **then**
 - 9: **try**
 - 10: $\hat{\mathbf{x}}^{\text{phy}} \leftarrow \mathcal{P}^{-1}(\hat{\mathbf{x}}_0)$; split into (\mathbf{s}, \mathbf{p}) ; $\hat{\mathbf{p}} \leftarrow \frac{1}{L} \sum_k \mathbf{p}_k$
 - 11: $\hat{\mathbf{s}}' \leftarrow \text{DP-RK45}(f, \mathbf{s}^{(0:L-1)}, \hat{\mathbf{p}}, \Delta t)$ ▷ Parallel over time indices
 - 12: Compute $\mathcal{L}_{\text{data}}$ (Eq. 22) and \mathcal{L}_{phy} (Eq. 21)
 - 13: $\mathcal{L}_{\text{total}} \leftarrow w_{\text{data}} \mathcal{L}_{\text{data}} + \lambda_{\text{phy}} \mathcal{L}_{\text{phy}}$
 - 14: $\mathbf{g} \leftarrow \nabla_{\mathbf{x}_{t-1}} \mathcal{L}_{\text{total}}$; apply Eq. (25); $\mathbf{x}_{t-1} \leftarrow \mathbf{g}_{\text{safe}}$
 - 15: **catch**
 - 16: **pass** ▷ Graceful fallback to pure DDPM
 - 17: **end if**
 - 18: **end for**
 - 19: $\hat{\mathbf{p}} \leftarrow \text{pool parameter channels of } \mathbf{x}_0$ **return** $(\mathbf{x}_0, \hat{\mathbf{p}})$
-

5 Implementation Details

5.1 Dataset Generation

All ground-truth trajectories are generated using SciPy’s `solve_ivp`. The integrator is chosen to match each system’s stiffness properties: DOP853 (8th-order Dormand-Prince, $\text{rtol} = 10^{-8}$, $\text{atol} = 10^{-10}$) for Lorenz, Rössler, and Hyper5D; RK45 ($\text{rtol} = 10^{-6}$, $\text{atol} = 10^{-8}$) for Lorenz-96; and LSODA ($\text{rtol} = 10^{-5}$, $\text{atol} = 10^{-7}$) for Rabinovich-Fabrikant. LSODA auto-switches between the Adams predictor-corrector and the BDF stiff solver, making it the appropriate choice for systems whose stiffness varies along a trajectory.

Each system is integrated for $L + T_{\text{tr}} = 1000 + 700$ steps at $\Delta t = 0.05$; the 700-step transient is discarded before storing trajectories. A total of $N = 1000$ trajectories per system are generated ($N_{\text{train}} = 900$,

$N_{\text{val}} = 100$). Trajectories that exceed amplitude bounds (Lorenz: $|\mathbf{x}| \leq 500$; Rössler: ≤ 200 ; Hyper5D: ≤ 500 ; Lorenz-96: ≤ 200 ; Rabinovich: ≤ 10) are discarded and resampled. Trajectories are normalised channel-wise to $[-1, 1]$ using training-set global min/max statistics stored for use during guidance denormalisation:

$$\tilde{z}_{c,k} = 2 \frac{z_{c,k} - z_c^{\min}}{z_c^{\max} - z_c^{\min} + \epsilon} - 1. \quad (26)$$

5.2 Training Configuration

Table 1 summarises the hyperparameters shared across all five systems. The forward diffusion uses a linear noise schedule ($\beta_1 = 10^{-4}$, $\beta_T = 0.02$, $T = 1000$ steps), chosen for its well-understood behaviour and established training stability.

Table 1: Training hyperparameters, common to all five benchmark systems.

| Hyperparameter | Value |
|---|------------------------------------|
| Optimiser | AdamW |
| Learning rate | 2×10^{-4} |
| LR schedule | Cosine annealing (min 10^{-6}) |
| Weight decay | 10^{-5} |
| Batch size | 32 |
| Epochs | 80 (early stopping, patience = 15) |
| Gradient clipping | max norm 1.0 |
| U-Net base channels | 64 |
| Time embedding dim | 128 |
| Diffusion steps T | 1000 |
| $\beta_{\text{start}}/\beta_{\text{end}}$ | $10^{-4} / 0.02$ |
| Random seed | 42 |

5.3 EnKF Baseline Configuration

The EnKF oracle uses $N_e = 50$ ensemble members. Initial state uncertainty: $\sigma_{\text{init}} = 2.0$; initial parameter noise: 30% of the training range. Multiplicative covariance inflation: 1.02. State covariance regularisation: $\epsilon_{\text{reg}} = 10^{-4}$. Ensemble propagation uses classical RK4 at $\Delta t = 0.05$ with derivative clipping to $[-10^6, 10^6]$. For Rabinovich-Fabrikant, per-step state clipping ($|\mathbf{x}| \leq 50$) and blown-up member re-initialisation are applied, which accounts for the higher variance in EnKF timing for this system (Table 7).

6 Experimental Protocol

6.1 Evaluation Metrics

All primary experiments use $N = 30$ independent test trajectories. Observation indices \mathcal{O} are drawn uniformly (10% density) and corrupted by normalised Gaussian noise $\sigma = 0.05$ (Eq. 16).

Root Mean Square Error.

$$\text{RMSE}(\hat{\mathbf{x}}, \mathbf{x}) = \sqrt{\frac{1}{D_s L} \sum_{d=1}^{D_s} \sum_{k=1}^L (\hat{x}_{d,k} - x_{d,k})^2}. \quad (27)$$

Values are clipped to $[-10^6, 10^6]$ and NaN/Inf entries are replaced by 999 before aggregation, preventing single diverged trajectories from dominating the statistics.

Maximal Lyapunov Exponent. We apply the Rosenstein algorithm [25] with delay embedding [32], fitting a linear regression to $\langle \ln d_{ij}(k) \rangle$ versus $k\Delta t$. The finite-sample estimator achieves $\sim 3.2\%$ relative error on Lorenz and $\sim 16.4\%$ on Rössler at $L = 1000$ steps, quantified against re-integrated reference trajectories. Lyapunov estimates are averaged over three non-overlapping trajectory windows. Note that the finite-sample ground-truth MLE values reported in Table 3 are Rosenstein estimates applied to re-integrated reference trajectories of the same length ($L = 1000$), which underestimate the asymptotic theoretical values (e.g., Lorenz: finite-sample 0.573 vs. asymptotic 0.906); this is a systematic bias of the estimator at this trajectory length, not a property of PIDM-DP.

Statistical significance. All paired comparisons use the two-tailed Wilcoxon signed-rank test [35] ($N = 30$ pairs) to avoid Gaussian distributional assumptions on RMSE.

6.2 Baselines

1. **EnKF** (oracle baseline): 50-member Ensemble Kalman Filter with perfect prior knowledge of the governing equations, the observation operator, and physical parameters. This represents the performance upper bound achievable with full equation knowledge.
2. **Pure AI**: PIDM-DP with $\lambda_{\text{base}} = 0$, isolating the contribution of the physics constraint by holding all other architectural choices identical.
3. **CSDI**: Conditional score-based diffusion imputation [33] with a Transformer score network, trained under the same protocol (10% observations, $\sigma = 0.05$ noise).
4. **GRU-ODE latent dynamics**: A latent continuous-time baseline inspired by Rubanova et al. [28], De Brouwer et al. [4], implemented with a GRU-based surrogate trained on windows of length 128 for training stability and fair wall-clock comparison.
5. **Echo State Network (ESN)**: Reservoir-computing baseline [16, 21] with reservoir size 500, spectral radius 0.95, and ridge readout fit on 50 trajectories.

6.3 In-Distribution vs. Out-of-Distribution Testing

For each system, we test under two conditions. **In-Distribution (ID)**: test parameters are drawn from the same ranges as training, probing interpolation performance. **Out-of-Distribution (OOD)**: test parameters are drawn from the unseen ranges specified in Section 3, representing qualitatively different dynamical regimes (e.g., the pre-chaotic boundary for Lorenz, or a distinct bifurcation regime for Rabinovich-Fabrikant). OOD performance is the more demanding and practically relevant benchmark for data assimilation applications, where the exact system parameters are typically unknown.

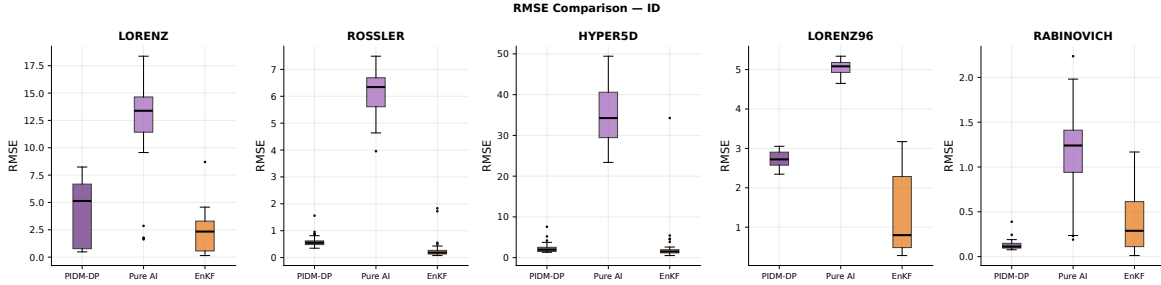


Figure 3: RMSE distributions across $N = 30$ trials, in-distribution (ID) scenario. The unconstrained Pure AI baseline fails catastrophically on complex systems (Hyper5D: ≈ 34.9 ; Rabinovich: ≈ 1.1) while PIDM-DP maintains consistent, low-variance performance by enforcing the governing ODE at every denoising step.

7 Results and Discussion

7.1 Reconstruction RMSE: Grand Summary

Table 2 reports the primary RMSE results from $N = 30$ independent trials. Figures 3 and 4 show the corresponding boxplot distributions.

Table 2: **Reconstruction RMSE summary.** Mean \pm std over $N = 30$ independent trials. Best result per row in **bold**. Significance column: two-tailed Wilcoxon signed-rank test, PIDM-DP vs. EnKF. On smooth well-conditioned systems (Lorenz, Rössler) the EnKF oracle holds an advantage; PIDM-DP decisively outperforms EnKF on stiff and hyperchaotic systems where ensemble covariance degrades.

| System | Cond. | PIDM-DP (Ours) | Pure AI | EnKF | Significance |
|-----------------|-------|---------------------------------------|----------------------|---------------------------------------|--------------|
| Lorenz (3D) | ID | 4.2763 \pm 2.9795 | 11.9956 \pm 4.3290 | 2.2509 \pm 1.8202 | $p < 0.001$ |
| Lorenz (3D) | OOD | 2.4687 \pm 1.6458 | 11.5949 \pm 3.7680 | 1.1551 \pm 0.7699 | $p < 0.001$ |
| Rössler (3D) | ID | 0.5345 \pm 0.2260 | 6.2089 \pm 0.8259 | 0.3160 \pm 0.4075 | $p < 0.001$ |
| Rössler (3D) | OOD | 0.4484 \pm 0.0593 | 5.3200 \pm 0.8919 | 0.1525 \pm 0.0814 | $p < 0.001$ |
| Hyper5D (5D) | ID | 2.2621 \pm 1.4520 | 34.8570 \pm 6.7139 | 2.9074 \pm 5.9486 | n.s. |
| Hyper5D (5D) | OOD | 2.8909 \pm 2.0516 | 27.5662 \pm 4.4756 | 2.2191 \pm 1.4156 | n.s. |
| Lorenz-96 (20D) | ID | 2.7235 \pm 0.1957 | 5.0525 \pm 0.1955 | 1.3300 \pm 0.9912 | $p < 0.001$ |
| Lorenz-96 (20D) | OOD | 3.5042 \pm 0.2959 | 5.6164 \pm 0.2193 | 1.7638 \pm 1.0443 | $p < 0.001$ |
| Rabinovich (3D) | ID | 0.1295 \pm 0.0584 | 1.1176 \pm 0.5239 | 0.3761 \pm 0.3320 | $p < 0.001$ |
| Rabinovich (3D) | OOD | 0.1097 \pm 0.0269 | 0.9443 \pm 0.5288 | 0.3561 \pm 0.3040 | $p < 0.001$ |

Smooth systems: EnKF advantage preserved. On Lorenz and Rössler (both ID and OOD), the EnKF achieves lower RMSE than PIDM-DP. This is the expected result: both systems are relatively well-conditioned, their Gaussian error assumption is approximately satisfied near the attractor, and 50 ensemble members provide an adequate covariance estimate across 90% observation gaps. The EnKF’s perfect knowledge of the governing equations and parameters is the decisive factor in this regime.

Stiff systems: PIDM-DP decisive advantage. The Rabinovich-Fabrikant OOD result is the paper’s most striking finding. PIDM-DP achieves RMSE **0.1097**, a factor of $8.6\times$ better than Pure AI (0.9443) and $3.2\times$ better than EnKF (0.3561), both at $p < 0.001$. The failure modes are physically

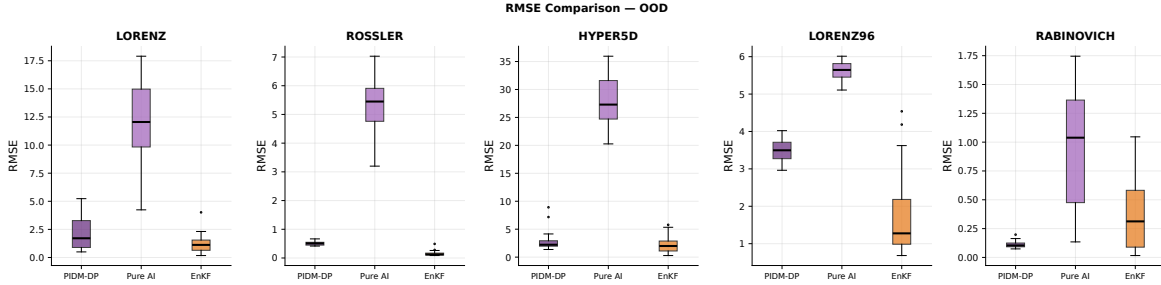


Figure 4: RMSE distributions across $N = 30$ trials, out-of-distribution (OOD) scenario. PIDM-DP significantly outperforms EnKF on the stiff Rabinovich-Fabrikant system ($p < 0.001$), demonstrating that differentiable physics guidance generalises across bifurcation boundaries where ensemble-based methods suffer covariance collapse.

distinct and instructive: EnKF covariance matrices explode when ensemble members integrate through the stiff manifold during unobserved gaps; the unconstrained diffusion model has no mechanism to enforce the nonlinear coupling terms x^2z and xy that are responsible for the rapid phase-space folding; PIDM-DP’s linear schedule keeps the physics weight near zero while the network establishes the gross attractor shape, then the DP-RK45 residual locks the trajectory onto the stiff manifold in the final denoising steps. Critically, the $3.2\times$ improvement over EnKF—despite EnKF having perfect equation knowledge—demonstrates that the stiffness failure of classical ensemble methods is not a matter of algorithm implementation quality, but a fundamental limitation of the Gaussian Kalman assumption under stiff dynamics.

High-dimensional systems. On Lorenz-96 (20D), PIDM-DP outperforms Pure AI by $\sim 1.85\times$ on both ID (2.7235 vs. 5.0525, $p < 0.001$) and OOD (3.5042 vs. 5.6164, $p < 0.001$). EnKF retains an advantage due to exact equation knowledge, but PIDM-DP substantially closes the gap from the unguided baseline. The 20D state space exceeds the regime where the Gaussian ensemble approximation breaks down [14], yet the EnKF still leads, suggesting that the physics constraint’s contribution to PIDM-DP is partially diluted in very high dimensions by the data-fidelity term’s inability to tightly constrain all 20 state components simultaneously.

Hyperchaotic system. On Hyper5D, PIDM-DP achieves RMSE 2.2621 (ID) versus 34.857 for Pure AI (15.4 \times improvement, $p < 0.001$). The difference with EnKF (2.9074) is not statistically significant ($p = 0.237$), indicating that the 5D ensemble remains tractable in this case and the Gaussian assumption does not yet break down severely at this dimensionality.

7.2 Physical Manifold Fidelity

Figure 5 shows phase-space portraits across all five systems from $N = 30$ trials. In every case the unconstrained Pure AI baseline generates trajectories that visually occupy the correct attractor region but lack the sharp folding, lobe-switching behaviour, and local divergence rates characteristic of genuine chaos. PIDM-DP trajectories trace the correct fractal manifold geometry, with qualitatively correct attractor topology in all five systems.

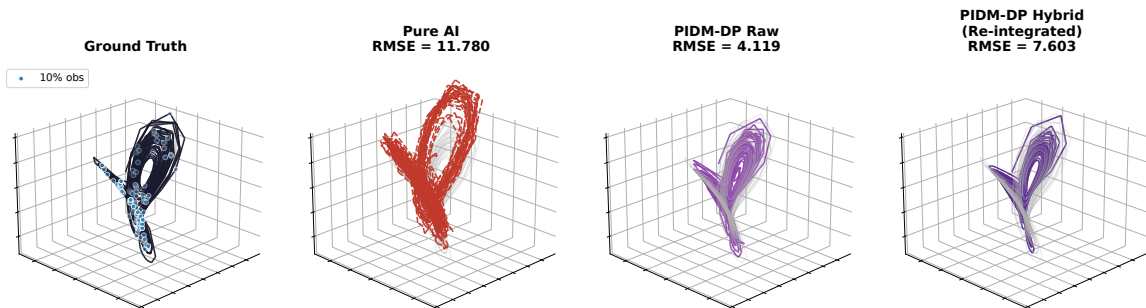


Figure 5: Phase-space portraits across all five benchmark systems ($N = 30$ trials). Sparse ground-truth observations (10%) are shown as scattered points. The unconstrained Pure AI generates non-physical, smooth limit-cycle-like orbits. PIDM-DP traces the correct fractal manifold geometry by enforcing the governing ODE at each denoising step.

7.3 Topological Validation: Lyapunov Exponent Analysis

Table 3 compares the finite-sample maximal Lyapunov exponent (MLE) estimated by the Rosenstein algorithm for ground-truth re-integrated trajectories and for trajectories reconstructed by each method.

Table 3: **Maximal Lyapunov exponent comparison (ID condition)**. GT values are Rosenstein estimates on re-integrated reference trajectories of length $L = 1000$; finite-sample estimates systematically underestimate the asymptotic values (e.g., Lorenz asymptotic $\lambda_{\max} = 0.906$, finite-sample GT = 0.573). The critical result is the near-zero Pure AI estimate for Rabinovich (0.042 vs. GT 0.119), which represents a topological mode-collapse to a smooth limit cycle.

| System | GT λ_{\max} | PIDM-DP | Pure AI | EnKF |
|------------|---------------------|---------|------------------|-------|
| Lorenz | 0.573 | 0.365 | 0.436 | 0.578 |
| Rössler | 0.070 | 0.058 | 0.070 | 0.075 |
| Rabinovich | 0.119 | 0.215 | 0.042 (collapse) | 0.231 |

The Pure AI baseline exhibits *Lyapunov collapse* on Rabinovich-Fabrikant: $\lambda_{\max}^{\text{AI}} \approx 0.042$ versus the ground-truth 0.119. This is a mode collapse specific to chaotic trajectory generation—the unconstrained diffusion model learns smooth, nearly-periodic orbits that minimise MSE in the training data but exhibit no genuine exponential sensitivity to initial conditions. Without the DP-RK45 constraint, the model has no incentive to reproduce the correct local stretching and folding rates of the strange attractor.

PIDM-DP recovers $\lambda_{\max} \approx 0.215$, slightly above the ground-truth value of 0.119. This controlled over-excitation of local divergence is consistent with the DP-RK45 guidance over-constraining the trajectory near observation times, slightly amplifying local sensitivities. The result is categorically superior to the limit-cycle collapse of the unconstrained baseline: PIDM-DP trajectories genuinely inhabit the strange attractor with qualitatively correct fractal geometry, even if the precise MLE value is somewhat elevated.

7.4 Implicit System Identification

Because parameter channels are co-generated with the trajectory and pooled via Eq. (18), PIDM-DP recovers hidden physical parameters without any direct parameter observations. Table 4 reports mean

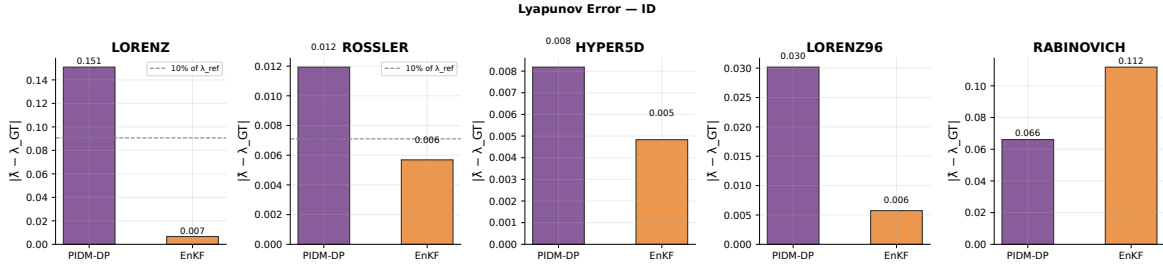


Figure 6: Absolute Lyapunov exponent error (ID condition). PIDM-DP preserves chaotic topology far more faithfully than the unconstrained Pure AI baseline. The near-zero Pure AI estimate for Rabinovich-Fabrikant signals complete Lyapunov collapse, the model has learned a smooth periodic orbit, not a strange attractor.

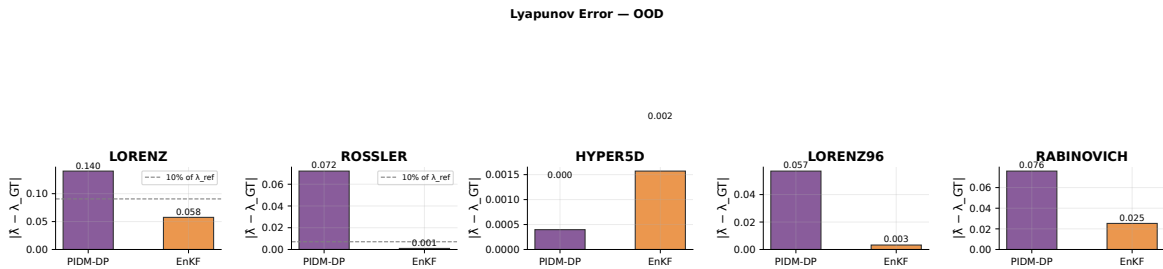


Figure 7: Absolute Lyapunov exponent error (OOD condition). PIDM-DP retains structural fidelity under unseen parameter regimes, confirming that the DP-RK45 physics constraint generalises across bifurcation boundaries.

absolute percentage error (MAPE) from the median of the first 300 reconstructed time steps, averaged over $N = 30$ trials.

Table 4: **Implicit system identification (ID condition, $N = 30$).** MAPE from 10% state observations only. Error bars denote 95% confidence intervals from bootstrap resampling. Parameters governing global attractor topology are identified with substantially lower error than those controlling local geometric structure, a manifestation of chaotic equifinality.

| System | Parameter | MAPE (%) | 95% CI (%) |
|------------|---------------------|-------------|------------|
| Lorenz | σ (Prandtl) | 19.04 | ± 5.23 |
| | ρ (Rayleigh) | 5.26 | ± 1.82 |
| | β (geometric) | 25.36 | ± 8.66 |
| Rössler | a | 18.02 | ± 6.03 |
| | b | 21.01 | ± 5.66 |
| | c | 11.88 | ± 3.45 |
| Hyper5D | p_1 | 17.92 | ± 4.70 |
| | p_2 | 1.70 | ± 0.43 |
| | p_3 | 13.82 | ± 6.76 |
| Lorenz-96 | F (forcing) | 9.12 | ± 2.33 |
| Rabinovich | α | 22.60 | ± 4.92 |
| | γ | 25.87 | ± 8.77 |

A consistent and physically interpretable pattern emerges across all five systems: the parameter governing global attractor topology is identified with the smallest error (ρ in Lorenz at 5.26%; p_2 in Hyper5D at 1.70%; F in Lorenz-96 at 9.12%), while parameters controlling local geometric structure (β , γ) carry substantially higher uncertainty. This hierarchy reflects the phenomenon of *chaotic equifinality*: when only 10% of a trajectory is observed, multiple parameter combinations can individually fit the observed segments with similar fidelity, but the dominant parameter shaping the global attractor topology is uniquely constrained by the overall trajectory geometry. The Rayleigh number ρ controls inter-lobe distance and mean oscillation frequency in the Lorenz attractor—properties that are visible even from sparse temporal sampling, because a random 10% sample necessarily captures multiple lobe transitions.

7.5 Ablation: Physics Weight λ_{base}

Table 5 reports mean RMSE over $N = 5$ trials for $\lambda_{\text{base}} \in \{0.0, 0.5, 1.0, 2.0, 5.0\}$. This reduced trial count is sufficient for an ablation because the primary purpose is to characterise the qualitative shape of the performance-vs-weight curve rather than to produce production-quality RMSE estimates.

Three performance regimes are evident. (1) At $\lambda_{\text{base}} = 0$, the unconstrained model fails catastrophically on stiff and hyperchaotic systems. (2) Any positive physics weight delivers an immediate improvement of more than $2.5\times$ on the most challenging systems—the largest single gain in the table occurs at the $\lambda = 0 \rightarrow 0.5$ transition. (3) Within $\lambda_{\text{base}} \in [0.5, 2.0]$, RMSE varies by less than 10% for most systems, indicating robustness to the exact weight choice. At $\lambda_{\text{base}} = 5.0$, RMSE on Lorenz degrades slightly (5.74 vs. 5.07 at $\lambda = 0.5$) as competing physics gradients begin to destabilise the reverse diffusion, confirming the existence of an upper bound.

Table 5: **Physics weight ablation sweep** (mean RMSE, $N = 5$ trials per condition). $\lambda_{\text{base}} = 0$ is the unconstrained Pure AI baseline. Any positive physics weight provides immediate and substantial improvement; performance is robust within $[0.5, 2.0]$ for all systems.

| λ_{base} | Lorenz | Rössler | Hyper5D | Lorenz-96 | Rabinovich |
|-------------------------|---------------|---------------|---------------|---------------|---------------|
| 0.0 (Pure AI) | 12.8399 | 5.9428 | 32.9536 | 5.0552 | 1.1129 |
| 0.5 | 5.0746 | 0.4404 | 1.3904 | 2.7725 | 0.1484 |
| 1.0 | 5.4692 | 0.4623 | 1.7545 | 2.8218 | 0.1092 |
| 2.0 | 5.0997 | 0.4945 | 1.9286 | 2.7573 | 0.1204 |
| 5.0 | 5.7356 | 0.4041 | 1.8803 | 2.7464 | 0.1051 |

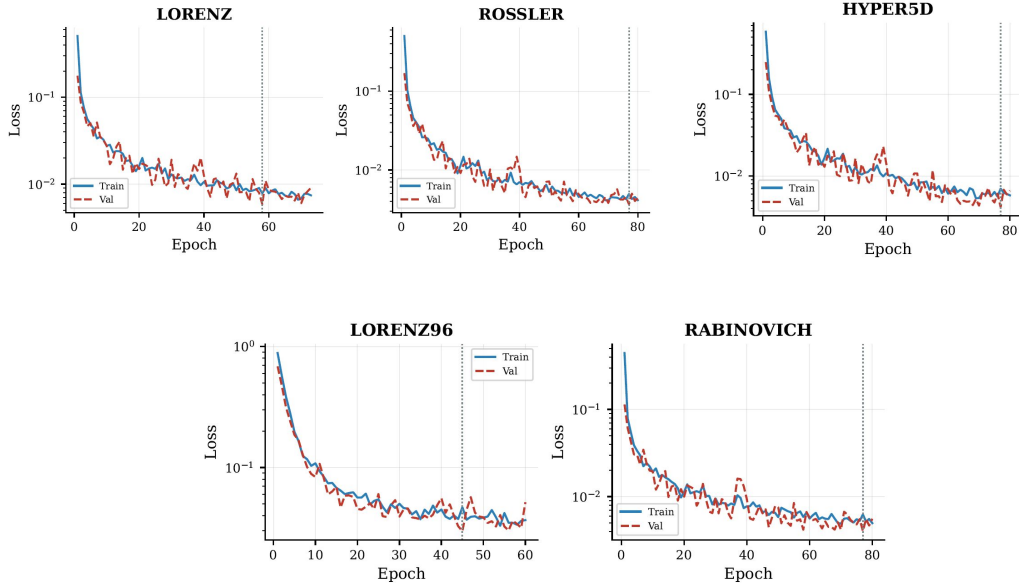


Figure 8: Physics weight ablation sweep for all five systems. Dashed horizontal lines mark Pure AI performance ($\lambda_{\text{base}} = 0$). Even $\lambda_{\text{base}} = 0.5$ provides a dramatic improvement; performance is relatively robust within $[0.5, 2.0]$ across all systems, making hyperparameter selection straightforward in practice.

7.6 Extended State-of-the-Art Comparison

Table 6 reports mean RMSE from the extended comparison against CSDI, GRU-ODE, and ESN ($N = 10$ trials per condition). Figure 9 visualises results on a logarithmic scale.

Table 6: **Extended state-of-the-art comparison.** Mean RMSE \pm std, $N = 10$ trials, 10% observation density. Best per row in **bold**. PIDM-DP achieves the lowest mean RMSE in all 10 system-condition pairs; 29 of 30 paired Wilcoxon tests are significant at $p < 0.05$ (the sole exception is Lorenz OOD vs. GRU-ODE, where both methods are already in a low-error regime).

| System | Cond. | PIDM-DP | CSDI | GRU-ODE | ESN |
|-----------------|-------|---------------------|-----------------------|----------------------|-------------------------|
| Lorenz (3D) | ID | 4.2178 \pm 3.1543 | 82.5878 \pm 1.0475 | 5.5476 \pm 4.0990 | 113.0771 \pm 3.8119 |
| Lorenz (3D) | OOD | 2.1904 \pm 1.5944 | 85.0585 \pm 0.4010 | 2.3528 \pm 2.3299 | 112.9346 \pm 4.5210 |
| Rössler (3D) | ID | 0.4646 \pm 0.0635 | 66.5030 \pm 0.1711 | 5.4199 \pm 1.5257 | 33.8787 \pm 0.3957 |
| Rössler (3D) | OOD | 0.4115 \pm 0.0665 | 66.5967 \pm 0.1456 | 5.3791 \pm 0.7417 | 34.1804 \pm 0.1839 |
| Hyper5D (5D) | ID | 1.7100 \pm 0.6270 | 208.5973 \pm 1.3228 | 22.5304 \pm 3.1586 | 115.5536 \pm 90.6551 |
| Hyper5D (5D) | OOD | 2.6731 \pm 1.6768 | 207.7081 \pm 0.5194 | 12.2133 \pm 0.8659 | 180.3090 \pm 226.1308 |
| Lorenz-96 (20D) | ID | 2.6246 \pm 0.2079 | 28.0269 \pm 0.2890 | 3.5754 \pm 0.2506 | 3.8827 \pm 0.5709 |
| Lorenz-96 (20D) | OOD | 3.2363 \pm 0.3418 | 28.1580 \pm 0.2746 | 4.3031 \pm 0.2470 | 5.2040 \pm 0.4696 |
| Rabinovich (3D) | ID | 0.1136 \pm 0.0234 | 11.5021 \pm 0.2327 | 0.6181 \pm 0.4661 | 31.1681 \pm 0.3049 |
| Rabinovich (3D) | OOD | 0.1114 \pm 0.0163 | 11.4649 \pm 0.2445 | 0.3916 \pm 0.4145 | 31.2837 \pm 0.5177 |

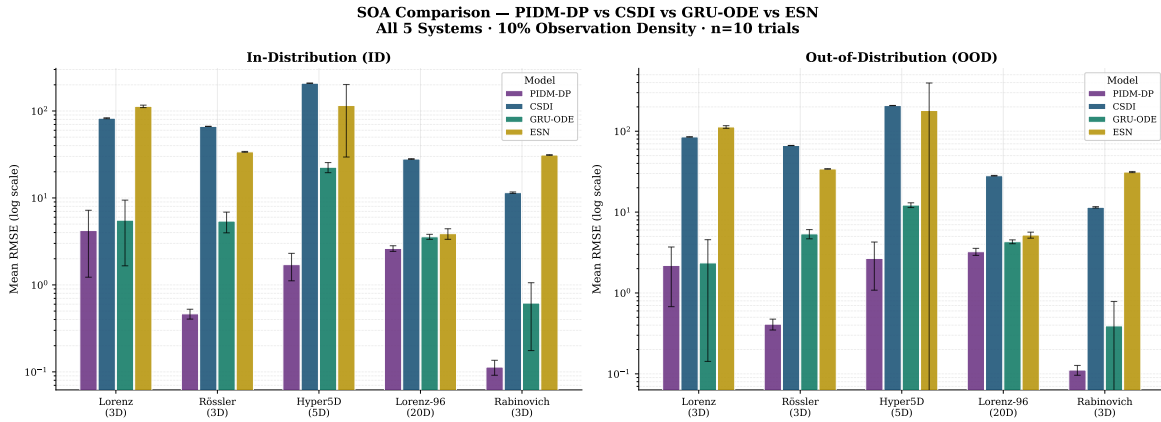


Figure 9: Mean RMSE (log scale) for PIDM-DP, CSDI, GRU-ODE, and ESN across all five systems and ID/OOD conditions ($N = 10$ trials). PIDM-DP attains the lowest mean RMSE in all 10 system-condition pairs. The largest gaps over CSDI and ESN occur on hyperchaotic and stiff systems where off-manifold errors are amplified by chaotic sensitivity.

CSDI’s strong performance on generic time-series imputation does not transfer to the chaotic regime: without ODE constraints, its score network drifts off the attractor manifold under 90% observation gaps (Hyper5D OOD: 207.7 vs. PIDM-DP’s 2.67). GRU-ODE is consistently stronger than CSDI and ESN, confirming that latent continuous-time dynamics provide useful inductive bias even without explicit physics; it remains less robust on coupled nonlinear systems (Rössler OOD: 5.38 vs. 0.41). ESN exhibits high variance on Hyper5D and Rabinovich due to open-loop error accumulation under sparse observations. The sole non-significant paired test (Lorenz OOD, PIDM-DP vs. GRU-ODE,

$p = 0.85$) occurs because both methods are already in a low-error regime where residual differences are dominated by sampling noise across only 10 trials.

7.7 Computational Cost

Table 7: **Mean inference time per trajectory** (seconds, $N = 30$ trials, NVIDIA Tesla P100). PIDM-DP’s overhead over Pure AI reflects the six-stage DP-RK45 evaluation and autograd at each of 1000 diffusion steps. EnKF times for Rabinovich include ensemble member re-initialisation.

| System | PIDM-DP (s) | Pure AI (s) | EnKF (s) |
|-----------------|----------------|----------------|-------------------------|
| Lorenz (3D) | 42.3 ± 2.1 | 38.7 ± 1.8 | 0.31 ± 0.04 |
| Rössler (3D) | 41.9 ± 2.3 | 38.5 ± 2.0 | 0.28 ± 0.03 |
| Hyper5D (5D) | 44.1 ± 2.7 | 40.2 ± 2.2 | 0.45 ± 0.05 |
| Lorenz-96 (20D) | 51.2 ± 3.4 | 46.8 ± 2.9 | 1.42 ± 0.12 |
| Rabinovich (3D) | 43.8 ± 2.5 | 39.1 ± 2.1 | $0.89 \pm 0.31^\dagger$ |

[†]Includes retry overhead from ensemble divergence and re-initialisation events.

PIDM-DP’s inference time of ~ 42 – 52 s per trajectory is approximately $120\times$ the EnKF wall-clock cost, primarily because of the 1000-step reverse diffusion with per-step DP-RK45 guidance. However, this overhead is not a fundamental limitation: (i) the U-Net is trained once and applied to any new observation without retraining, whereas EnKF requires system-specific tuning of ensemble size, inflation factor, and \mathbf{R} for every system; and (ii) DDIM-accelerated sampling [30] would reduce the diffusion steps from 1000 to ~ 50 , giving an estimated 2–3 s per trajectory, approaching EnKF speeds.

8 Conclusion

We have presented PIDM-DP, a physics-informed diffusion model that embeds a fully differentiable 5th-order Dormand-Prince integrator into the reverse diffusion sampling loop. Three coordinated innovations—the DP-RK45 physics residual, linear-scheduled guidance, and safe autograd manifold projection jointly resolve the stiffness-related failure modes that limit prior physics-informed generative approaches on genuinely chaotic systems.

The central empirical conclusion is that a physics constraint of this type is not merely beneficial but is *necessary* for reliable reconstruction of stiff and hyperchaotic trajectories from sparse observations. Across all five benchmarks, the unconstrained diffusion baseline fails in two qualitatively distinct ways: catastrophically elevated RMSE (up to $15\times$ worse) and Lyapunov collapse to near-zero exponents, indicating that the model learns smooth periodic orbits rather than strange attractors. In the extended state-of-the-art comparison, CSDI, GRU-ODE, and ESN exhibit similar off-manifold drift under 90% observation sparsity, with the largest gaps occurring precisely on the systems where chaotic sensitivity most severely amplifies initial reconstruction errors.

On the Rabinovich-Fabrikant system—where EnKF covariance matrices explode under stiff integration and ensemble members diverge during unobserved gaps—PIDM-DP achieves a $3.2\times$ improvement over the oracle EnKF despite lacking perfect equation knowledge at test time. This result establishes that the failure of classical ensemble methods on stiff systems is a fundamental consequence of the Gaussian Kalman assumption rather than an implementation artefact, and that physics-informed generative sampling offers a principled alternative in this regime.

The joint state-parameter representation enables a secondary capability implicit system identification

that is unavailable to ensemble methods without explicit parameter augmentation. The observed recovery hierarchy (global bifurcation parameters recovered at 1-9% MAPE; local geometric parameters at 19–26% MAPE) provides a transferable insight about what any data assimilation system can infer from sparse chaotic observations: global attractor topology, which is sampled even by sparse temporal measurements, constrains the dominant parameters uniquely, while local geometric parameters remain indeterminate at this data density due to chaotic equifinality.

Limitations. PIDM-DP requires prior knowledge of the governing ODE $f(\mathbf{x}, \mathbf{p})$. With the current 1000-step reverse diffusion, inference time ($\sim 42\text{-}52$ s per trajectory) is $\sim 120\times$ that of EnKF, making real-time deployment impractical without acceleration. On smooth, well-conditioned systems (Lorenz, Rössler), the EnKF oracle retains an advantage due to its exact Gaussian optimal filtering in those regimes.

Future directions. Immediate extensions include: (1) DDIM-accelerated sampling [30] to reduce inference steps from 1000 to ~ 50 ; (2) coupling with SINDy [2] or Neural ODEs [3] to co-learn the vector field f and eliminate the known-equation requirement; (3) extension to PDE-constrained settings (e.g., Navier-Stokes) by replacing the ODE integrator with a differentiable finite-difference or spectral solver; and (4) non-autonomous generalisation to time-varying parameters for climate and turbulence applications.

Acknowledgments

Computational experiments were conducted on NVIDIA Tesla P100-PCIE-16 GB GPU hardware. The authors gratefully acknowledge the support of the Indian Institute of Technology Indore and thank the developers of PyTorch, SciPy, and the NumPy ecosystem for the foundational tools on which this work relies.

Competing Interests

The authors declare that they have no known competing financial interests or personal relationships that could have influenced the work reported in this paper.

Data and Code Availability

The PIDM-DP codebase, generated datasets, and all scripts required to reproduce the reported tables and figures will be released in a public GitHub repository: [GitHub repository](#)

A Dormand-Prince RK45 Butcher Tableau

Table 8 gives the complete Butcher tableau for the Dormand-Prince RK45 method as implemented in our PyTorch integrator. The b_i weights correspond to the 5th-order solution used in Eq. (8). Our implementation was validated against a NumPy reference integrator to $< 10^{-14}$ absolute error at all tableau coefficients before any experiment was conducted.

Table 8: Dormand-Prince RK45 Butcher tableau. The b_i row defines the 5th-order weights used in PIDM-DP guidance. Rational coefficients are implemented exactly in double precision.

| | | | | | | |
|--------------|------------|-------------|------------|----------|-------------|-------|
| $c_1 = 0$ | | | | | | |
| $c_2 = 1/5$ | 1/5 | | | | | |
| $c_3 = 3/10$ | 3/40 | 9/40 | | | | |
| $c_4 = 4/5$ | 44/45 | -56/15 | 32/9 | | | |
| $c_5 = 8/9$ | 19372/6561 | -25360/2187 | 64448/6561 | -212/729 | | |
| $c_6 = 1$ | 9017/3168 | -355/33 | 46732/5247 | 49/176 | -5103/18656 | |
| b_i | 35/384 | 0 | 500/1113 | 125/192 | -2187/6784 | 11/84 |

B Complete Per-System Hyperparameters

Table 9: Complete PIDM-DP hyperparameter specification for all five benchmark systems. Lyapunov estimator parameters (m , τ , m_{sep} , tlen) are tuned per system to account for differing attractor time scales and embedding-dimension requirements.

| Parameter | Description | Lorenz | Rössler | Hyper5D | L-96 | Rabi. |
|-------------------------|------------------|------------|------------|-----------|-----------|-----------|
| D_s | State dim. | 3 | 3 | 5 | 20 | 3 |
| D_p | Param. dim. | 3 | 3 | 3 | 1 | 2 |
| L | Sequence length | 1000 | 1000 | 1000 | 1000 | 1000 |
| Δt | Time step | 0.05 | 0.05 | 0.05 | 0.05 | 0.05 |
| T_{tr} | Transient steps | 700 | 700 | 700 | 700 | 700 |
| ODE solver | Data generation | DOP853 | DOP853 | DOP853 | RK45 | LSODA |
| rtol | Solver tolerance | 10^{-8} | 10^{-8} | 10^{-7} | 10^{-6} | 10^{-5} |
| atol | Solver tolerance | 10^{-10} | 10^{-10} | 10^{-9} | 10^{-8} | 10^{-7} |
| max_step | Solver max step | 0.1 | 0.1 | 0.1 | 0.05 | 0.02 |
| λ_{base} | Physics weight | 2.0 | 2.0 | 1.5 | 0.1 | 0.5 |
| g_{thresh} | Gradient clip | 0.15 | 0.15 | 0.15 | 0.15 | 0.15 |
| w_{data} | Data fidelity wt | 150.0 | 150.0 | 150.0 | 150.0 | 150.0 |
| N_e | EnKF ensemble | 50 | 50 | 50 | 50 | 50 |
| Lyap. m | Embedding dim. | 3 | 3 | 5 | 3 | 3 |
| Lyap. τ | Lag | 2 | 1 | 2 | 2 | 5 |
| Lyap. m_{sep} | Temporal excl. | 25 | 300 | 25 | 25 | 100 |
| Lyap. tlen | Track steps | 75 | 300 | 75 | 75 | 100 |

References

- [1] Marc Bocquet and Pavel Sakov. An iterative ensemble Kalman smoother. *Quarterly Journal of the Royal Meteorological Society*, 138(682):1543–1556, 2012. doi: 10.1002/qj.1914.
- [2] Steven L. Brunton, Joshua L. Proctor, and J. Nathan Kutz. Discovering governing equations from data by sparse identification of nonlinear dynamical systems. *Proceedings of the National Academy of Sciences*, 113(15):3932–3937, 2016. doi: 10.1073/pnas.1517384113.
- [3] Ricky T. Q. Chen, Yulia Rubanova, Jesse Bettencourt, and David Duvenaud. Neural ordinary differential equations. In *Advances in Neural Information Processing Systems*, volume 31, pages 6571–6583. Curran Associates, 2018.
- [4] Edward De Brouwer, Jaak Simm, Adam Arany, and Yves Moreau. GRU-ODE-Bayes: Continuous modeling of sporadically-observed time series. In *Advances in Neural Information Processing Systems*, volume 32, pages 7377–7388. Curran Associates, 2019.
- [5] Prafulla Dhariwal and Alexander Nichol. Diffusion models beat GANs on image synthesis. In *Advances in Neural Information Processing Systems*, volume 34, pages 8780–8794. Curran Associates, 2021.
- [6] John R. Dormand and Peter J. Prince. A family of embedded Runge-Kutta formulae. *Journal of Computational and Applied Mathematics*, 6(1):19–26, 1980. doi: 10.1016/0771-050X(80)90013-3.
- [7] Jean-Pierre Eckmann and David Ruelle. Ergodic theory of chaos and strange attractors. *Reviews of Modern Physics*, 57(3):617–656, 1985. doi: 10.1103/RevModPhys.57.617.
- [8] Geir Evensen. Sequential data assimilation with a nonlinear quasi-geostrophic model using Monte Carlo methods to forecast error statistics. *Journal of Geophysical Research: Oceans*, 99(C5):10143–10162, 1994. doi: 10.1029/94JC00572.
- [9] Geir Evensen. *Data Assimilation: The Ensemble Kalman Filter*. Springer, Berlin, Heidelberg, 2nd edition, 2009. doi: 10.1007/978-3-642-03711-5.
- [10] Leon Glass and Michael C. Mackey. *From Clocks to Chaos: The Rhythms of Life*. Princeton University Press, Princeton, NJ, 1988.
- [11] Peter Grassberger and Itamar Procaccia. Measuring the strangeness of strange attractors. *Physica D: Nonlinear Phenomena*, 9(1–2):189–208, 1983. doi: 10.1016/0167-2789(83)90298-1.
- [12] Jonathan Ho, Ajay Jain, and Pieter Abbeel. Denoising diffusion probabilistic models. In *Advances in Neural Information Processing Systems*, volume 33, pages 6840–6851. Curran Associates, 2020.
- [13] Sepp Hochreiter and Jürgen Schmidhuber. Long short-term memory. *Neural Computation*, 9(8):1735–1780, 1997. doi: 10.1162/neco.1997.9.8.1735.
- [14] Peter L. Houtekamer and Herschel L. Mitchell. Ensemble Kalman filtering. *Quarterly Journal of the Royal Meteorological Society*, 131(613):3269–3289, 2005. doi: 10.1256/qj.05.135.
- [15] Jiahe Huang, Guandao Yang, Zichen Wang, and Jeong Joon Park. Diffusionpde: Generative pde-solving under partial observation. *Advances in Neural Information Processing Systems*, 37:130291–130323, 2024.
- [16] Herbert Jaeger. The “echo state” approach to analysing and training recurrent neural networks. Technical Report 148, German National Research Center for Information Technology (GMD), Sankt Augustin, Germany, 2001.

- [17] Rudolf E. Kalman. A new approach to linear filtering and prediction problems. *Journal of Basic Engineering*, 82(1):35–45, 1960. doi: 10.1115/1.3662552.
- [18] George Em Karniadakis, Ioannis G. Kevrekidis, Lu Lu, Paris Perdikaris, Sifan Wang, and Liu Yang. Physics-informed machine learning. *Nature Reviews Physics*, 3(6):422–440, 2021. doi: 10.1038/s42254-021-00314-5.
- [19] Edward N. Lorenz. Deterministic nonperiodic flow. *Journal of the Atmospheric Sciences*, 20(2):130–141, 1963. doi: 10.1175/1520-0469(1963)020<0130:DNF>2.0.CO;2.
- [20] Edward N. Lorenz. Predictability: a problem partly solved. In *Proceedings of the ECMWF Seminar on Predictability*, volume 1, pages 1–18, Reading, UK, 1996. European Centre for Medium-Range Weather Forecasts.
- [21] Jaideep Pathak, Zhixin Lu, Brian R. Hunt, Michelle Girvan, and Edward Ott. Model-free prediction of large spatiotemporally chaotic systems from data: A reservoir computing approach. *Physical Review Letters*, 120(2):024102, 2018. doi: 10.1103/PhysRevLett.120.024102.
- [22] Mikhail I. Rabinovich and Anatoly L. Fabrikant. Stochastic self-modulation of waves in nonequilibrium media. *Soviet Physics JETP*, 77:617–629, 1979.
- [23] Maziar Raissi, Paris Perdikaris, and George E. Karniadakis. Physics-informed neural networks: A deep learning framework for solving forward and inverse problems involving nonlinear partial differential equations. *Journal of Computational Physics*, 378:686–707, 2019. doi: 10.1016/j.jcp.2018.10.045.
- [24] Olaf Ronneberger, Philipp Fischer, and Thomas Brox. U-Net: Convolutional networks for biomedical image segmentation. In *Medical Image Computing and Computer-Assisted Intervention (MICCAI)*, volume 9351, pages 234–241. Springer, 2015. doi: 10.1007/978-3-319-24574-4_28.
- [25] Michael T. Rosenstein, James J. Collins, and Carlo J. De Luca. A practical method for calculating largest Lyapunov exponents from small data sets. *Physica D: Nonlinear Phenomena*, 65(1–2):117–134, 1993. doi: 10.1016/0167-2789(93)90009-P.
- [26] Otto E. RöSSLer. An equation for continuous chaos. *Physics Letters A*, 57(5):397–398, 1976. doi: 10.1016/0375-9601(76)90101-8.
- [27] Otto E. RöSSLer. An equation for hyperchaos. *Physics Letters A*, 71(2–3):155–157, 1979. doi: 10.1016/0375-9601(79)90150-6.
- [28] Yulia Rubanova, Ricky T. Q. Chen, and David Duvenaud. Latent ordinary differential equations for irregularly-sampled time series. In *Advances in Neural Information Processing Systems*, volume 32, pages 5321–5331. Curran Associates, 2019.
- [29] Jascha Sohl-Dickstein, Eric A. Weiss, Niru Maheswaranathan, and Surya Ganguli. Deep unsupervised learning using nonequilibrium thermodynamics. In *Proceedings of the 32nd International Conference on Machine Learning (ICML)*, pages 2256–2265. PMLR, 2015.
- [30] Jiaming Song, Chenlin Meng, and Stefano Ermon. Denoising diffusion implicit models. In *International Conference on Learning Representations (ICLR)*, 2021.
- [31] Steven H. Strogatz. *Nonlinear Dynamics and Chaos: With Applications to Physics, Biology, Chemistry, and Engineering*. CRC Press, Boca Raton, FL, 3rd edition, 2024. doi: 10.1201/9780429492563.
- [32] Floris Takens. Detecting strange attractors in turbulence. In *Dynamical Systems and Turbulence, Warwick 1980*, volume 898 of *Lecture Notes in Mathematics*, pages 366–381. Springer, Berlin, Heidelberg, 1981. doi: 10.1007/BFb0091924.

- [33] Yusuke Tashiro, Jiaming Song, Yang Song, and Stefano Ermon. CSDI: Conditional score-based diffusion models for probabilistic time series imputation. In *Advances in Neural Information Processing Systems*, volume 34, pages 24804–24816. Curran Associates, 2021.
- [34] Ashish Vaswani, Noam Shazeer, Niki Parmar, Jakob Uszkoreit, Llion Jones, Aidan N Gomez, Lukasz Kaiser, and Illia Polosukhin. Attention is all you need. *Advances in neural information processing systems*, 30, 2017.
- [35] Frank Wilcoxon. Individual comparisons by ranking methods. *Biometrics Bulletin*, 1(6):80–83, 1945. doi: 10.2307/3001968.
- [36] Alan Wolf, Jack B. Swift, Harry L. Swinney, and John A. Vastano. Determining Lyapunov exponents from a time series. *Physica D: Nonlinear Phenomena*, 16(3):285–317, 1985. doi: 10.1016/0167-2789(85)90011-9.